Static Characteristics of VCSELs and PIN Photodiodes for Bidirectional Standard Multimode Fiber Transmission

Alexander Kern and Dietmar Wahl

We present the monolithic design, fabrication and static properties of 850 nm wavelength AlGaAs–GaAs-based transceiver chips with a stacked layer structure of a VCSEL and a PIN photodetector. Bidirectional data transmission via a single, two-side butt-coupled multimode fiber (MMF) is thus enabled. The approach aims at a miniaturization of transceiver chips in order to ensure compatibility with standard MMFs with core diameters of 50 and 62.5 μm used predominantly in premises networks. These chips are supposed to be well suited for low-cost and compact half- and full-duplex interconnection at Gbit/s data rates over distances of a few hundred meters.

1. Introduction

Owing to the increasing penetration of optical interconnection into mobile systems, local industrial networks and nowadays also into the home environment, compact and low-cost transceivers are more and more needed. A possible way to satisfy this demand is a transceiver chip which consists of a vertical-cavity surface-emitting laser (VCSEL) sharing the chip area with an intimately integrated photodetector. The monolithic integration of both components as well as a design avoiding the use of external optics saves space, weight and module cost.

So far there have been several examples of monolithic integration of a VCSEL and a photodetector for optical interconnection purposes. An interesting attempt to use a VCSEL as an efficient laser source and a resonant-cavity-enhanced avalanche photodetector is introduced in [1]. Such a dual-purpose device is switched between two operation modes. Half-duplex operation at 1.25 Gbit/s data rate over a 50 μm core diameter MMF with 500 m length was demonstrated. Full-duplex data transmission is possible in case of spatial separation of both devices. Similar to [1], just one epitaxial layer structure for a VCSEL can be used in order to fabricate monolithically integrated transceivers consisting of a VCSEL and a resonant photodetector [2]. Unfortunately such solutions are not well suited for low-cost links owing to resonant detection, which requires temperature control at both fiber ends due to the very narrow spectral range of the photodetector. Non-resonant detection is achieved by the employment of separate epitaxial layers for photodiode and VCSEL [3, 4]. Usually such a transceiver is grown in one run and thus contains all the epitaxial layers from the beginning. Both the vertical and horizontal separation of the devices is achieved by means of lithography and selective etching techniques.

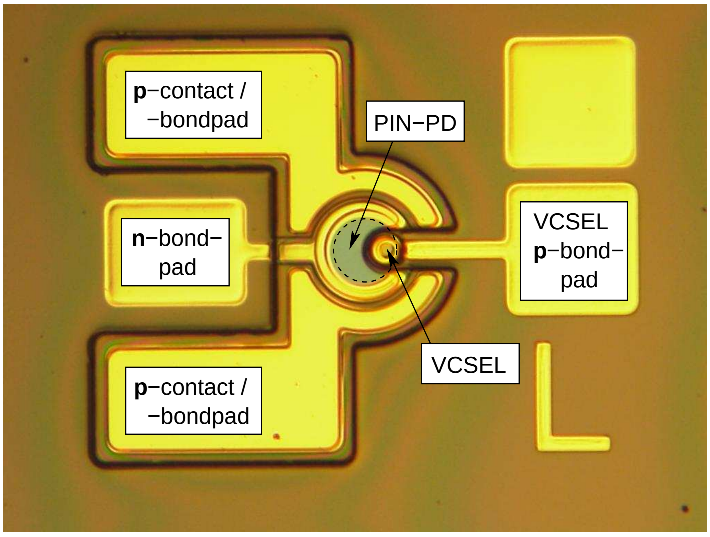

Fig. 1: Photograph of a transceiver chip consisting of a VCSEL and a 60 µm diameter PIN PD. The VCSEL is positioned off-center with respect to the photodetector in order to maximize the effective photodetecting area of the transceiver. The dashed line indicates the alignment of a MMF with 50 µm core diameter.

In recent years, we have shown several designs of monolithically integrated VCSELs and GaAs-based metal–semiconductor–metal (MSM) photodiodes [5]. Since MSM photodiodes generally have lower responsivities due to their metal contact fingers that partially shadow the detector area, PIN-type photodiodes are predestined for applications implying reduced fiber core diameters. Matching the transceiver chips to standard MMFs requires further miniaturization of the VCSEL in order to maximize the photosensitive area of the integrated chip. Figure 1 shows a transceiver chip with a 60 µm PIN PD and a laterally integrated VCSEL.

2. Chip Layout and Processing

A monolithically integrated transceiver chip comprises all epitaxial layers necessary for signal generation and detection. Figure 2 illustrates schematically such a layer structure grown by molecular beam epitaxy.

2.1 VCSEL

The layers for the PIN photodetector are grown on top of the VCSEL layers, separated by a 150 nm thick $Al_{0.9}Ga_{0.1}As$ etch stop layer. The resonator of the VCSEL is built by a n-type doped bottom Bragg mirror containing 38.5 $Al_{0.2}Ga_{0.8}As/Al_{0.9}Ga_{0.1}As$ periods grown on a n-doped GaAs substrate and 23 equivalent p-type top mirror pairs. The inner cavity has an optical thickness of one wavelength and contains three 8 nm thick GaAs quantum wells, separated by 10 nm $Al_{0.27}Ga_{0.73}As$ barrier layers. A 32 nm thick p-doped AlAs layer in the first top mirror period above the active region is designated for current

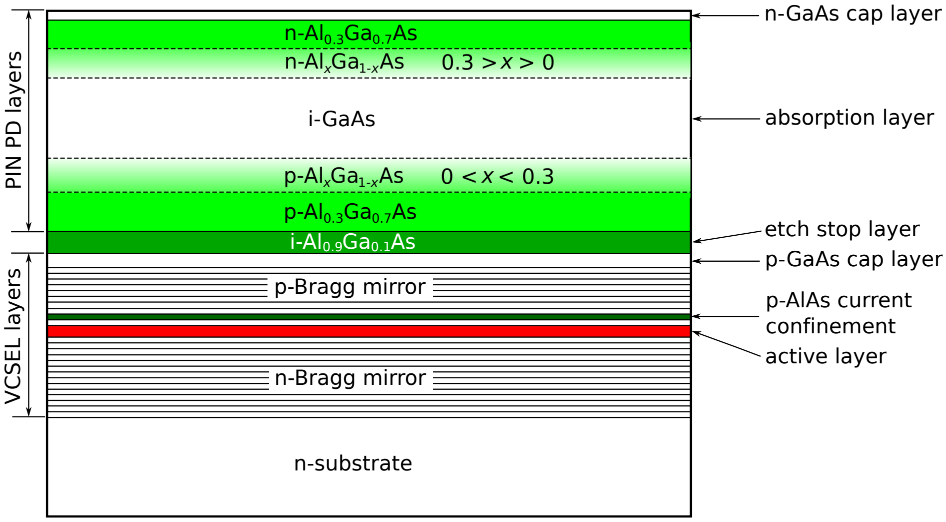

Fig. 2: Schematic layer structure of the transceiver chip. The layers for the PIN PD on top of the VCSEL layers are separated by an etch stop layer.

confinement after an oxidation step. The VCSEL growth is terminated with a 30 nm highly p-doped GaAs layer, which provides a low-resistance p-contact and at the same time prevents oxidation of the subjacent aluminum containing layers.

2.2 PIN PD

The PIN photodiode is grown on top of the intrinsic etch stop layer, which also partially acts as an insulator by reducing capacitive coupling between the two devices. The 1 μm thick undoped GaAs absorption layer is sandwiched by p- and n-doped $Al_{0.3}Ga_{0.7}As$. The higher bandgap energy of these two contact layers provides a window for the wavelengths of interest at around 850 nm. In order to minimize the energy band discontinuities between the absorption and contact layers, linearly graded n- and p-$Al_xGa_{1-x}As$ ($x = 0 \rightarrow 0.3$) is employed, ensuring an easier escape of the light-induced carriers from the undoped GaAs. The 10 nm thick n-doped GaAs cap layer protects the subjacent n-$Al_{0.3}Ga_{0.7}As$ from oxidation.

2.3 Fabrication

The fabrication of transceiver chips is based on lithographic structuring with photosensitive resists and subsequent etching or material deposition steps. Seven to eight lithographic steps are necessary for the full processing of the transceiver chip shown in Fig. 3. In the first step, the detector layers on top of the VCSEL are removed by a selective reactive-ion etching (RIE) process. In order to ensure that the uppermost VCSEL layer is not affected by the etching, it is protected by an etch stop layer with a high aluminum content, as mentioned above. Combining dry-etching processes with $SiCl_4$ alone and with appropriate $SF_6/SiCl_4$ ratio, high etching selectivities between GaAs and $Al_xGa_{1-x}As$

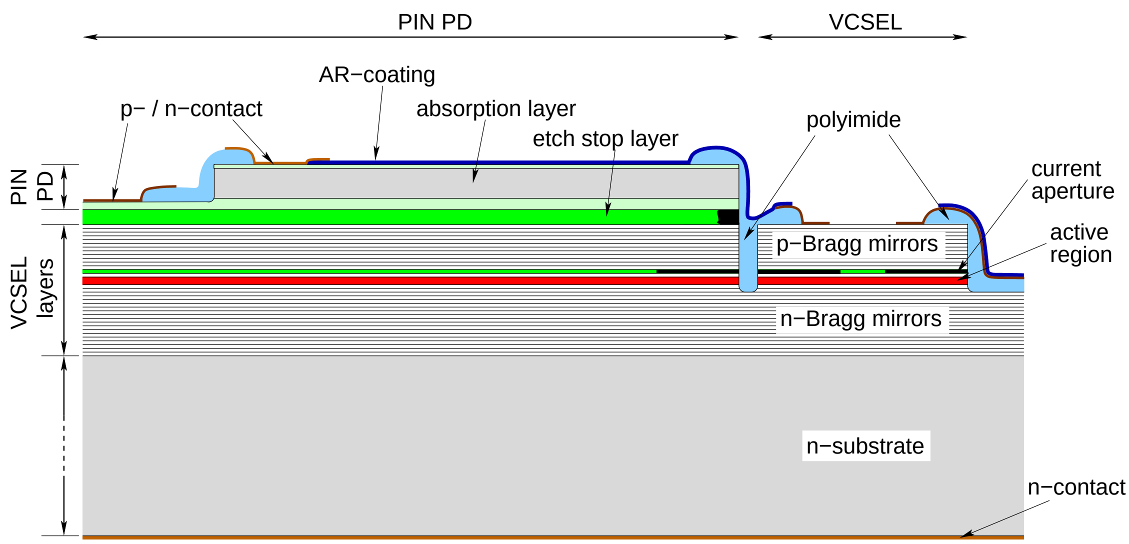

Fig. 3: Schematic layer structure of the transceiver chip. The layers for the PIN PD on top of the VCSEL layers are separated by an etch stop layer.

layers can be achieved [6], thus terminating the dry-etching on the $Al_{0.9}Ga_{0.1}As$ layer. Followed by a selective wet-etching with hydrofluoric acid, the highly p-doped cap layer of the VCSEL can now be exposed. Unlike, e.g., MSM PDs with planar contact structure, PIN PDs have vertically displaced contacts and thus require an additional etch step to expose the p-doped $Al_{0.3}Ga_{0.7}As$ layer, as can be seen in the left part of Fig. 3. With increased $SF_6/SiCl_4$ ratio, the selective dry-etching process can also be adapted to layers with lower aluminum content [6]. By means of the described selective etching techniques, a uniform layer topography all over the wafer can be guaranteed in spite of the intentional layer thickness inhomogeneity due to the epitaxial growth process. The third etching process spatially separates the VCSEL and the photodetector by a 2–4 µm narrow trench and gives access to the current confinement layer, as seen in the right part of Fig. 3. It is performed just with $SiCl_4$ without selectivity. Also this process step requires reactive-ion etching due to its steep mesa sidewalls, which are crucial for the miniaturization and dense integration of the VCSEL and PIN PD. Selective oxidation in a hot water vapor atmosphere forms the current aperture in the AlAs layer. An aluminum content of 90 % in the 150 nm thick etch stop layer ensures only a moderate oxidation rate compared to the current confinement layer [7]. A deep oxidation of the etch stop layer associated with a volume change would induce strain in the surrounding layers, which could cause cracks and damage of the PD's edges after the subsequent annealing process for the n-contacts. On the other hand, a low aluminum content could result in a lower etching selectivity of the hydrofluoric acid. The fourth lithography step provides planarization and passivation with polyimide. Afterwards, both p- and n-contacts of the PD and VCSEL are evaporated and annealed, in order to form low-resistance contacts. As can be seen in the left part of Fig. 1, the bondpad arrangement of the PD allows testing with a microwave probe. The VCSEL is driven via the bondpad of the p-contact and the back side n-contact on the substrate. In the last lithography step, an Al_2O_3 quarter-wave antireflection (AR)

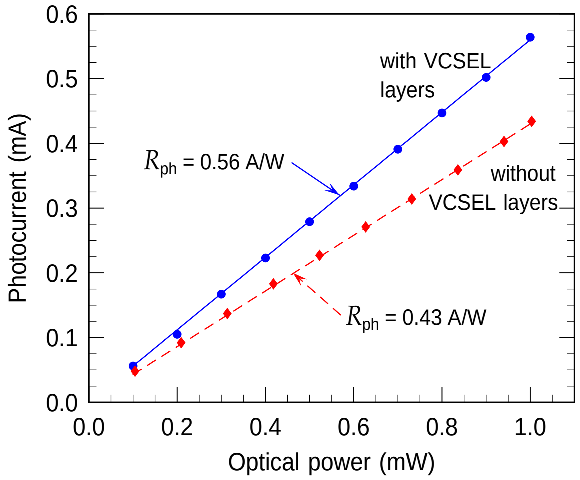

Fig. 4: Photocurrent of a PIN PD with 60 µm diameter biased at 3 V as a function of the incident optical power at 850 nm wavelength. The measurements were carried out with two samples with and without VCSEL layers underneath the PIN PD.

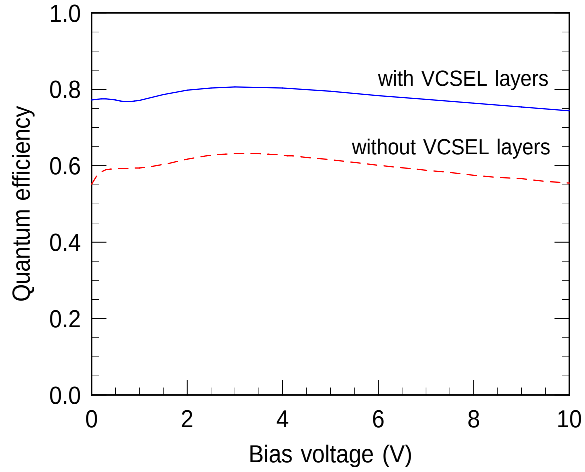

Fig. 5: Quantum efficiencies of PIN PDs from Fig. 4 dependent on the reverse bias voltage. The maximum quantum efficiency is achieved for both samples at a bias voltage of about 3 V.

layer is sputtered on the area of the transceiver chip which is exposed to incident light. The reflectivity of the semiconductor surface is thus reduced from approximately 30 % to 1.3 % over a spectral width of nearly 50 nm [5].

3. Device Measurements

3.1 Basic PIN PD characteristics

The VCSEL as well as the PIN photodiode are designed for operation at 850 nm. For photodiode characterization, the beam of a reference laser diode was focused on an AR-coated full-area circular photodetector with 60 µm diameter reverse biased at 3 V. Both the sample containing only the PIN layers and the sample including all transceiver layers, i.e., VCSEL and PIN PD, were used in order to study possible influences of the underlying VCSEL layers. In Fig. 4, the relation between the generated photocurrent I_{ph} and the corresponding incident optical power P_{opt} is shown. The power was varied with an optical attenuator in order to keep the operating current constant and thus to avoid a thermally induced wavelength drift of the reference laser. The responsivity

$$R_{\mathrm{ph}} = \frac{I_{\mathrm{ph}}}{P_{\mathrm{opt}}} \tag{1}$$

of the two devices can be determined from the slope of the strongly linear curves. The device with only the PIN layers has a responsivity of 0.43 A/W. The theoretical value of 0.41 A/W is 5 % lower and includes only a simple single-pass absorption with an absorption coefficient of 9000 cm^{-1} for high-purity GaAs at 850 nm [8]. In this case, around 59 % of the incident optical power is absorbed by the 1 µm thick GaAs absorption layer. The measured responsivity of the sample with a complete transceiver structure reaches 0.56 A/W. The 30 % higher responsivity arises from the subjacent VCSEL structure, where almost all of the non-absorbed intensity is reflected and thus passes the absorption region for a second time. The calculated responsivity of 0.57 A/W considers a simple double-pass absorption or just a single propagation through a twice as thick absorption layer and is a good approximation to the measured value. The higher measured value for the device with only the PIN layers could instead occur from a rather weak backreflection of the underlying structure, which was not considered in the calculation.

The responsivity of a photodetector introduced by (1) can also be expressed as

$$R_{\mathrm{ph}} = \eta \frac{q}{h\nu} = \eta \frac{\lambda}{1.24\,\mu\mathrm{m}} \frac{\mathrm{A}}{\mathrm{W}}\,, \tag{2}$$

including its quantum efficiency η, Planck's constant h, the elementary charge q, the light frequency ν, and the wavelength λ. In Fig. 5, the quantum efficiency extracted from the photocurrent measurements according to (1) and (2) is presented as a function of the bias voltage. The dependence is indeed weak, nevertheless the maximum value of a quantum efficiency of 81 % for the sample with underlying VCSEL Bragg mirrors and 63 % for the photodiode with single-pass absorption is reached at around 3 V bias voltage. The quantum efficiency is [9]

$$\eta = (1 - R) \cdot (1 - \exp\{-\alpha d\})\,, \tag{3}$$

in which $R = 1.3\,\%$ is the reflection coefficient of the AR-coated PD [5], d the thickness of the absorption layer and $\alpha = 9000\,\mathrm{cm}^{-1}$ the absorption coefficient of pure GaAs at 850 nm according to [8]. In (3) the absorption in the p- and n-regions of the PIN PD is neglected due to the higher bandgap of $Al_{0.3}Ga_{0.7}As$. The calculated value of about 82 % for the complete transceiver is close to the experimental data. The lower theoretical value of 59 % for the sample without the VCSEL layers could indicate a certain reflection of the non-absorbed light by the underlying p- and etch stop layer. The approach of single-pass absorption has to be taken with some care.

3.2 Basic VCSEL characteristics

The transmitting element of the transceiver chip is a standard top-emitting, oxide-confined, predominantly multimode VCSEL operating in the 850 nm wavelength range. For optimization and evaluation purposes, three VCSEL sizes were implied in the lithography mask design. The fully processed sample contains transceivers with different VCSEL mesa diameters of 22, 25, and 28 µm. For instance, Fig. 1 shows a transceiver chip with a 28 µm VCSEL and a 60 µm PD. The operation characteristics of the three VCSELs from the same sample, correspondingly having different oxide aperture diameters, are displayed in Fig. 6. Multimode operation is observed using devices with 7.8 and 4.5 µm oxide aperture with maximum optical output powers of 10.3 and 6.6 mW at thermal rollover, respectively. The smallest device with an oxide aperture of just 1.5 µm, on the other hand, shows single-mode operation with a maximum optical power of 1.9 mW. The

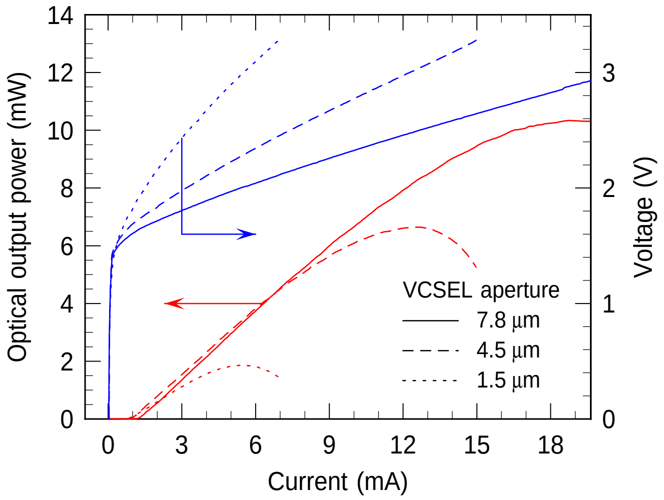

Fig. 6: Continuous-wave light–current–voltage characteristics of GaAs VCSELs with three different oxide aperture diameters at room temperature.

largest VCSEL has a threshold current of 1.3 mA and a differential quantum efficiency of 54 %. The device with a current aperture of 4.5 µm shows similar values of 1 mA and 51 %. In contrast, the smallest VCSEL has 1 mA threshold current but only 34 % differential quantum efficiency. Higher scattering losses at the oxide aperture are a likely reason. The differential resistances extracted by linear interpolation of the current–voltage characteristics at high operating currents are 235, 104, and 65 Ω for 22, 25, and 28 µm VCSEL mesas, respectively.

4. Conclusion

In this article, a new kind of monolithically integrated 850 nm wavelength transceiver chip has been presented for bidirectional optical data transmission over standard multimode fibers. The chips consist of PIN photodiodes and oxide-confined, top-emitting VCSELs, integrated to match 50 and 62.5 µm core diameter GI MMFs. The miniaturization versus previous generations of VCSEL/MSM PD chips requires the establishment of new fabrication processes and thus also new epitaxial layer designs. The crucial point of the seven lithography steps are the dry-etching processes, which define the PD plateau and expose the p-contact layer of the PIN photodetector and VCSEL. The etching selectivity for the $Al_xGa_{1-x}As$ layers can be adjusted with an appropriate choice of the $SF_6/SiCl_4$ gas ratio in the RIE machine.

The PIN photodiode with 1 µm thick absorption layer has a responsivity of 0.43 A/W for single-pass absorption. For the complete transceiver layer structure, the responsivity is enhanced by 30 % to 0.56 A/W, which is due to the reflection of the non-absorbed light at the underlying VCSEL layers and thus a double-pass absorption. The quantum efficiency of the transceiver-type PIN PD is 81 %, whereas the single-pass PD has 63 %. Oxide-confined VCSELs with 7.8 µm current aperture diameter show maximum optical output powers of 10.3 mW, threshold currents below 1.3 mA, and 54 % differential quantum efficiency.

Investigations into the dynamic properties of complete transceiver chips are in progress. We expect a lot of room for improvements with optimized layer structures and processing. Half- and full-duplex data transmission experiments over different multimode fibers will be performed in the near future.

References

[1] J.D. Ingham, R.V. Penty, and I.H. White, "Bidirectional multimode-fiber communication links using dual-purpose vertical-cavity devices", *J. Lightwave Technol.*, vol. 24, pp. 1283–1294, 2006.

[2] O. Sjölund, D.A. Louderback, E.R. Hegblom, J. Ko, and L.A. Coldren, "Individually optimized bottom-emitting vertical-cavity lasers and bottom-illuminated resonant photodetectors sharing the same epitaxial structure", *J. Opt. A: Pure Appl. Opt.*, vol. 1, pp. 317–319, 1999.

[3] A.M. Kasten, A.V. Giannopoulos, C. Long, C. Chen, and K.D. Choquette, "Fabrication and characterization of individually addressable vertical-cavity surface-emitting laser arrays and integrated VCSEL/PIN detector arrays", in *Vertical Cavity Surface Emitting Lasers XI*, K.D. Choquette, J.K. Guenter (Eds.), Proc. SPIE 6484, pp. 64840C-1–6, 2007.

[4] P. Kazlas, J. Wasserbauer, J. Scott, D. Paananen, S. Swirhun, and D. Lewis, "Monolithic vertical-cavity laser/p-i-n photodiode transceiver array for optical interconnects", *IEEE Photon. Technol. Lett.*, vol. 10, pp. 1530–1532, 1998.

[5] R. Michalzik, A. Kern, M. Stach, F. Rinaldi, and D. Wahl, "True bidirectional optical interconnects over multimode fiber", in *Optoelectronic Interconnects and Component Integration IX*, A.L. Glebov, R.T. Chen (Eds.), Proc. SPIE 7607, pp. 76070B-1–17, 2010.

[6] S. Salimian and C.B. Cooper, III, "Selective dry etching of GaAs over AlGaAs in $SF_6/SiCl_4$ mixtures", *J. Vac. Sci. Technol. B*, vol. 6, pp. 1641–1644, 1988.

[7] K.D. Choquette, R.P. Schneider, Jr., K.L. Lear, and K.M. Geib, "Low threshold voltage vertical-cavity lasers fabricated by selective oxidation", *Electron. Lett.*, vol. 30, pp. 2043–2044, 1994.

[8] H.C. Casey, Jr., D.D. Sell, and K.W. Wecht, "Concentration dependence of the absorption coefficient for n- and p-type GaAs between 1.3 and 1.6 eV", *J. Appl. Phys.*, vol. 46, pp. 250–257, 1975.

[9] K.J. Ebeling, *Integrated Optoelectronics*, Berlin: Springer-Verlag, 1993.